ACTA METALLURGICA SINICA (ENGLISH LETTERS)
Vol. 8 No. 4—6 pp 553 – 562 August – December 1995

Shape-Memory Intermetallics Development in Taiwan

S.K. Wu
Institute of Materials Science and Engineering, National Taiwan University
Taipei, Taiwan 106, China
H.C. Lin
Department of Materials Science, Feng-Chia University, Taichung,
Taiwan 407, China

In Taiwan, many groups engage in the development of TiNi SMAs. The two-stage martensitic transformations of B2↔R-phase↔B19′ and B2↔B19↔B19′ have been clarified for both TiNi binary and ternary alloys. The deformation behaviors have been investigated by cold-rolling, hot-rolling and wire drawing. Both shape memory effect and pseudoelasticity can be improved by some thermal-mechanical treatments. The damping characteristics of TiNi and TiNiX SMAs have also been systematically studied. Both B19′/B19 martensite (M) and R-phase (R) have high damping capacities due to the stress-induced movement of twin boundaries. Meanwhile, the addition of third elements — Fe and Cu — can largely increase the damping capacity. Recently, some high temperature shape memory alloys — TiNiPd and TiNi-Au alloys — have also been intensively studied in Taiwan. All these potential investigations on the TiNi SMAs in Taiwan have attracted much attention and their important characteristics will be applied widely in the near future.

KEY WORDS *TiNi shape memory alloys, research and development in Taiwan*

Symbols

B2, R, B19, B19′ — *cubic, rhombohedral, orthorhomic and monoclinic structure, respectively.*
Ms(Mf), As(Af) — *forward and reverse martensitic transformation temperatures, respectively, in the electrical resistivity tests,* ℃
M^*, A^* — *forward and reverse martensitic transformation temperatures, respectively, in the DSC measurements,* ℃.
T_R, T_R^* — *forward and reverse R-phase transformation tempertures, respectively, in the electrical resistivity tests and DSC measurements*
P_{C1}, P_{H1} — *forward and reverse martensitic transformation temperatures, respectively, in the internal friction tests,* ℃
To — *equilibrium temperature,* ℃
$\triangle H$ — *heat of transformation,* Jg^{-1}
$\triangle W$ — *energy loss in a strain cycle*
Q^{-1} — *internal friction value,* $Q^{-1} = \xi = \delta / \pi$
ξ — *damping ratio*
δ — *logarithmic decrement of strain amplitude*
E — *mechanical energy*
σ — *stress, MPa*
ε — *strain*
K — *constant*

TiNi alloys are known as the most important shape memory alloys (SMAs) because of many applications based on their shape memory effect (SME)[1], pseudoelasticity (PE)[2, 3] and high damping capacity (HDC)[4, 5]. This comes from the fact that TiNi alloys have superior properties in ductility, strength, fatigue, corrosion resistance, recoverable strain, etc. In Taiwan, there are many groups engaging in the development of TiNi SMAs, including Taiwan University, Tsing-Hua University, Feng-Chia University, Chung-Shan Institute of Science and Technology, etc. The main investigations are on the crystallography, transformation behaviors, thermal-mechanical treatments, manufacturing processes, and actual applications based on the characteristics of SME, PE and HDC.

1 Transformation Behaviors

1.1 B2↔R-phase↔B19' martensite

It is well known that the R-phase transformation can appear prior to the martensitic transformation after some treatments, such as: the addition of a ternary element[6], low temperature annealing treatments following cold work[7, 8], thermal cycling[9, 10] and aging of Ni-rich alloys[11~13]. Figure 1 shows that the $Ti_{49}Ni_{51}$ alloys aged at 400°C can exhibit the transformation sequence of B2↔R-phase↔martensite. In the early aging stage (Fig. 1(b)), only the R-phase transformation is observed due to the Ms point being deeply depressed by the coherent stress of $Ti_{11}Ni_{14}$ precipitates. In the later aging stage (Fig. 1(c)), internal friction peaks associated with R-phase and martensitic transformations are all observed on both heating and cooling cycles.

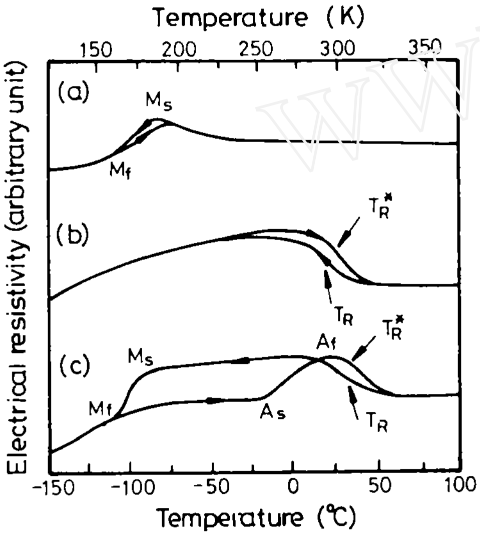

Fig. 1 Electrical resistivity vs. temperature curves for (a) 800 °C × 2h annealed and water quenched (solution treated) $Ti_{49}Ni_{51}$ alloy. (b) The same as (a), but now followed by the 400°C × 1h aged. (c) The same as (a), but now followed by the 400°C × 5h aged.

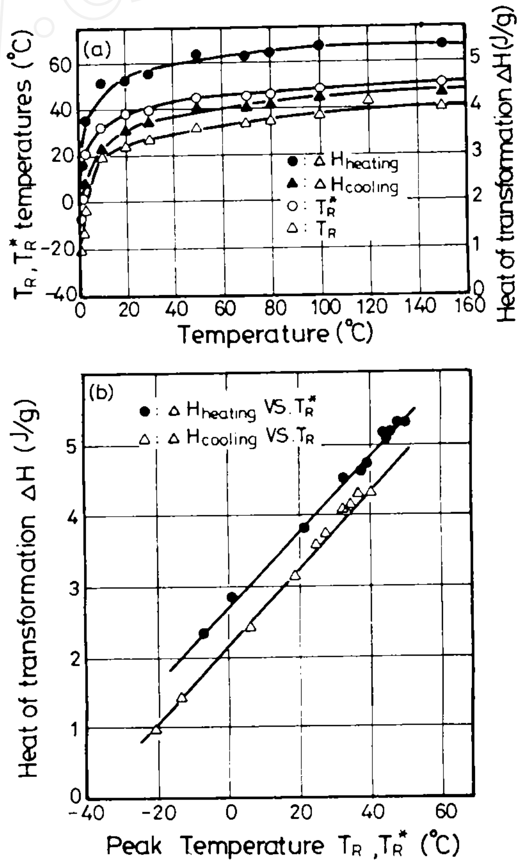

Fig. 2 (a) T_R, T_R^* and ΔH as a function of aging time. (b) ΔH as a function of transformation peak temperatures T_R and T_R^*.

In order to understand the variation of T_R, T^*_R (DSC peak temperatures associated with the R-phase transformation) and ΔH value with the aging time, and the relationship between ΔH and TR (T^*_R), $Ti_{49}Ni_{51}$ specimens are aged at 300°C for various periods of time and measured by the DSC. In Figure 2(a), all T_R, T^*_R and ΔH values increase quickly in the early aging, and then approach to some steady values. At the same time, in Figure 2(a), the variation of ΔH values with the aging time has the same tendency as that of T_R and T^*_R. Hence, a linear relationship between ΔH and T_R (T^*_R) is found in Figure 2(b). Based on the thermodynamic viewpoint, ΔH value is expected to be linearly related to the transformation temperature with the hypothesis that the transformation is "thermoelastic" in nature[14]. Hence, the results of Fig. 2(b) imply that the R-phase transformation has the characteristic of a "thermoelastic" transformation.

1.2 B2↔B19↔B19' martensite

The $Ti_{50}Ni_{40}Cu_{10}$ ternary alloy is reported to undergo a typical B2↔B19 and B19↔B19' two-stage martensitic transformation, where B2, B19 and B19' represent cubic, orthohombic and monoclinic structures, respectively. Figure 3 shows the results of DSC measurements in both forward and reverse transformations for $Ti_{50}Ni_{40}Cu_{10}$ alloy. For Fig 3, one can observe two DSC peaks which appear on each heating/cooling curve. The first transformation appearing at the higher temperature is accompanied with a significant heat effect, whereas the second transformation appearing at the lower temperature causes only a minor heat effect. These results contrast with those of electrical resistivity test (Fig. 4), internal friction measurement[15], where sharp peaks in the cooling and heating curves are known to be due to the B2↔B19 martensitic transformation and small peaks are associated with the B19↔B19' martensitic transformation. Figures 5(a-t) show the X-ray diffraction profiles of $Ti_{50}Ni_{40}Cu_{10}$ alloy, which were obtained at selected temperatures during successive cooling (a-j) and heating (k-t) sequences. As shown in Fig. 5, we suggest that the formation of B19' martensite is characterized by a monoclinic distortion of B19 martensite with respect to the obliqued $\bar{b}$ axis. The monoclinic angle β of B19' martensite increases with decreasing temperature from 95.8° at 260K to 97.2° at 20K. The characteristic of the continuously monoclinic distortion of B19' martensite is comparable with that of continuously rhombohedral distortion of R-phase[16, 17].

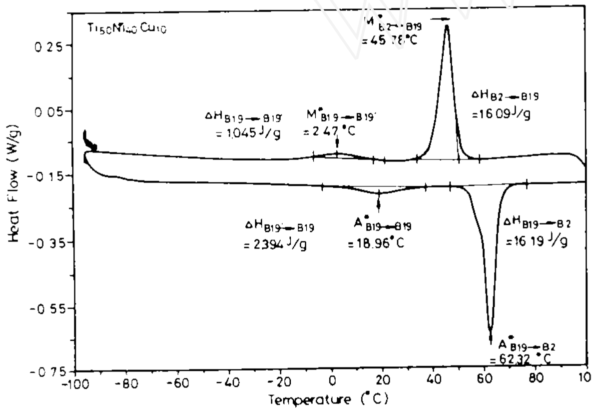

Fig. 3 DSC curves for $Ti_{50}Ni_{40}Cu_{10}$ alloy

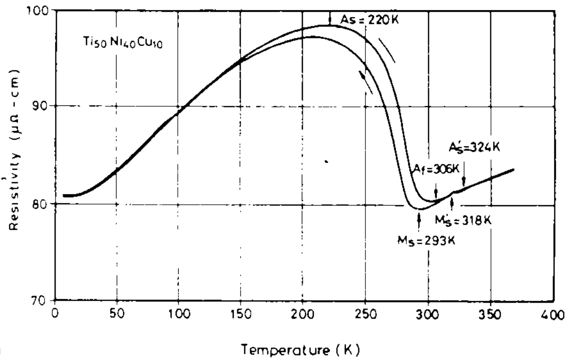

Fig. 4 Electrical resistivity vs. temperature curve of $Ti_{50}Ni_{50}Cu_{10}$ alloy

The internal friction measurement of $Ti_{50}Ni_{40}Cu_{10}$ alloy indicates that the shear modulus of B19 martensite has an unusually low value over a broad temperature range between the two shear modulus minima, i.e., in the temperature range of B19 martensite existence. The B2↔B19 transformation is thus proposed to proceed under the condition of deep shear modulus softening.

2. Deformation Behaviors

2.1 Cold-rolling

Figure 6 shows plots of internal friction Q^{-1} vs temperature for the 20% cold-rolled Ti50Ni50 alloy and here peaks P_{H1-1}, P_{C1} and P_{H1-2} are associated with the martensitic transformations. Similar results are obtained for other cold-rolled conditions. All peak temperatures of P_{H1-1}, P_{C1} and P_{H1-2} at various degrees of cold-rolling (thickness reduction) are plotted in Fig. 7. In Fig. 7 P_{H1-1}, P_{C1} and P_{H1-2} are strongly affected by cold rolling. The temperature of P_{H1-1} significantly increases, but on the contrary, P_{C1} and P_{H1-2} monotonously decrease, with the incereasing degree of cold rolling. The temperature increment of P_{H1-1} can reach 120°C for the 40% thickness-reduced specimen. Compared the temperature of P_{H1-1} to that of P_{H1-2}, the temperature increment due to the cold-rolling can substantially be annealed out. This result exhibits the phenomena of martensite stabilization. Namely, the normally reverse transformation can be prevented and the martensite phase can be "stabilized" by cold-rolling, therefore, the re-

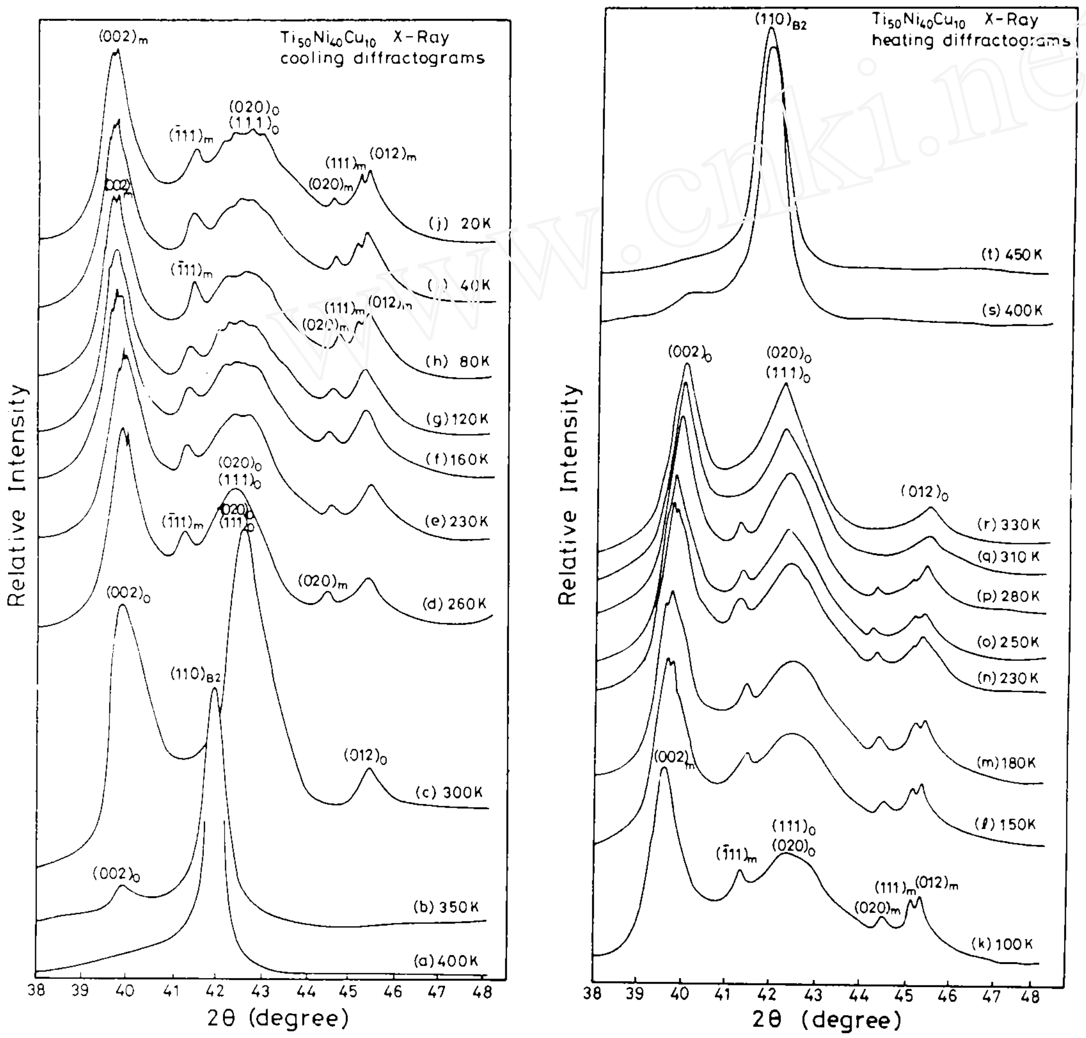

Fig. 5 X-ray diffraction profiles of Ti$_{50}$Ni$_{40}$Cu$_{10}$ alloy, which were obtained by successively cooling (a-j) and heating (k-t) the specimen. Subscripts "c", "o" and "m" of the diffraction peaks represent that they come from the B2, B19 and B19' phases respectively.

verse transformation temperatures, As and Af, shift to higher ones. Both deformed martensite structures and deform-induced dislocations/vacancies are considered to be related to the martensite stabilization. After the occurrence of the first reverse martensitic transformation of B19'↔B2, the martensite stabilization dies out and the transformation temperatures are depressed by retained dislocations on subsequent thermal cycles.

The tensile test shows that the martensite accommodation ⁄ reorientation process in the as cold-rolled equiatomic TiNi alloy is depressed due to the hindrance of deformed martensite structures and defects, as indicated in Fig. 8. If the cold-rolled equiatiomic TiNi alloy is subjected to a reverse martensitic transformation (RMT) at temperature $< 300^{\circ}C$, the strenghening effect induced by cold-rolling can sig-

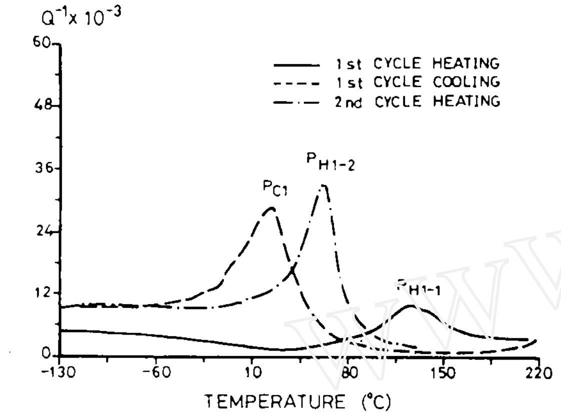

Fig 6 Internal friction vs. temperature curves for the 20% thickness-reduced $Ti_{50}Ni_{50}$ alloy with specimen thickness 1.04mm. Peaks P_{H1-1}, P_{C1} and P_{H1-2} are all associated with the martensitic transformation.

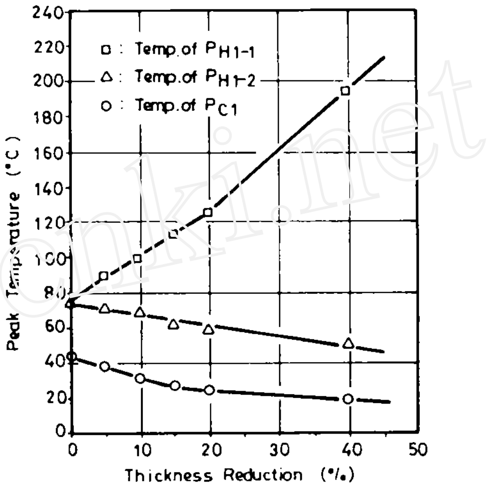

Fig. 7 Peak temperatures of P_{H1-1}, P_{C1} and P_{H1-2} vs. thickness reduction for the $Ti_{50}Ni_{50}$ alloy cold-rolled at room temperature

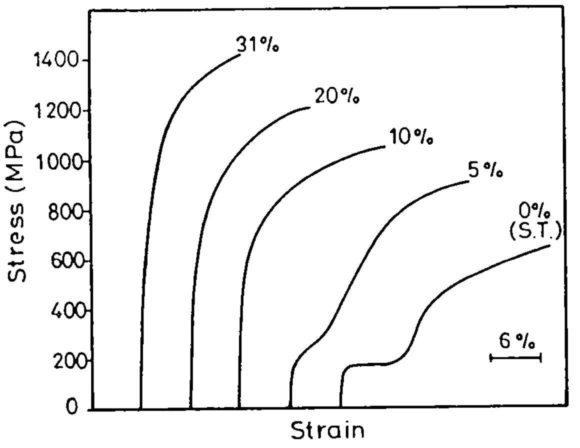

Fig. 8 Typical engineering stress vs. strain curves for solution-treated (S.T.) and S.T.+cold-rolled $Ti_{50}Ni_{50}$ specimens.

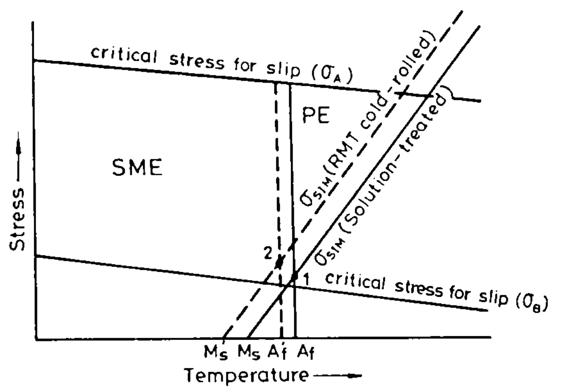

Fig. 9 Schematic diagram representing regions of SME and PE in stress-temperature coordinates for the RMT cold-rolled specimens

nificantly improve the alloy's characteristic SME and PE by raising the critical shear stress for slip. These effects can be summarized in the schematic diagram for Fig. 9. In Fig. 9, σ_A and σ_B are the critical resolved shear stresses for slip deformation in the alloy with and without a strengthening effect, respectively. If the applied stress exceeds the critical stress for slip deformaton (i.e. $\sigma_{apply} > \sigma_B$), residual strain is introduced and SME and PE are suppressed. However, if the critical slip stress of TiNi alloy is rasied by cold-rolling strengthening, (e.g. $\sigma_A > \sigma_B$ in Fig. 9),the permanent strain will be reduced and both SME and PE are improved. At the same time, Ms and A_f temperatures are depressed to Ms' and A_f' after the cold-rolling[18], hence, the oblique line exhibiting the critical stress for stress induced martensite (SIM) is shifted to the lower temperature side, as shown by dashed oblique line in Fig. 9. Beside, the vertical line separating the regions of PE and SME is also shifted to the lower temperature side, as shown by dashed vertical line in Fig. 9. This feature extends the PE applications to the lower temperature range and increases the minimum stress for inducing SIM, as indicated by marks 1 and 2. Meanwhile, as shown in Fig. 10 for the PE characteristic, a cold-rolled and then reversed martensitic transformation process conducted in TiNi SMAs can also increase signficantly their stored mechanical energy and the energy storage efficiency.

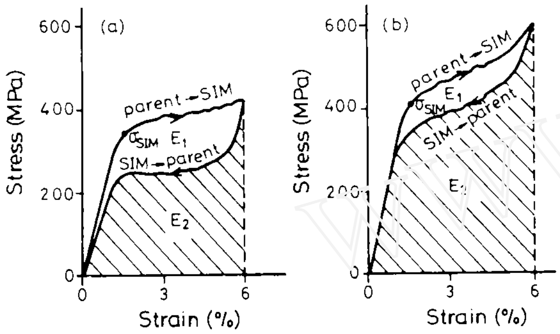

Fig. 10 The tensile stress-strain curves exhibiting the pseudoelasticity characeristics for (a) 10% thickness-reduced RMT, (b) 20% thickness-reduced RMT spcimens

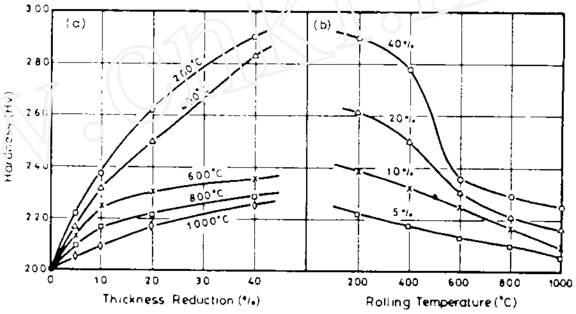

Fig. 11 (a) Hardness Hv vs. thickness reduction; (b) hardness Hv vs. rolling temperature for the hot-rolled $Ti_{50}Ni_{50}$ alloy

2.2 Hot-rolling

Both rolling temperature and thickness reduction have important influences on the work hardening and hardness of hot-rolled plates. The greater the thickness reduction, the more the number of retained dislocations, and therefore, the higher the rate of work hardening, as shown in Fig. 11. At rolling temperatures ≥600°C, recovery or recrystallization occurs. However, because of the short rolling time and the fast cooling rate in air, the recovery or recrystallization is incomplete. The peak temperatures M^* and A^* of DSC measurement are found to decrease with increasing thickness reduction and with decreasing rolling temperature. This feature is related to the retained dislocations induced by hot-rolling, as can be under stood from the inversely linear relationship between peak temperatures and the hardness Hv, Fig. 12. Namely, the effect of hot rolling on martensitic transfromation temperatures follows the equation[19]:

$$Ms - To \quad K\Delta\sigma y \tag{1}$$

Here, the yield stress $\Delta\sigma y$ of hot-rolled specimen is regarded as being proportional to its hardness.

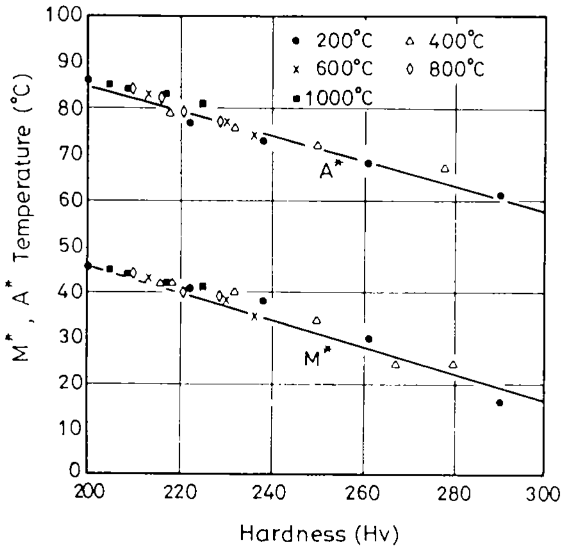

Fig. 12 M* and A* temperatures vs. hardness Hv for the hot-rolled $Ti_{50}Ni_{50}$ alloy

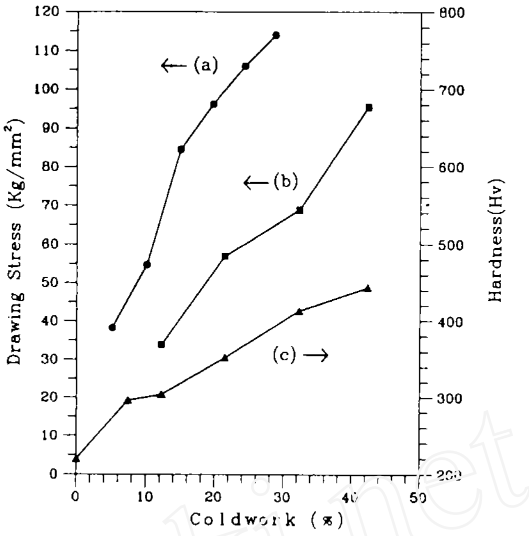

Fig. 13 (a) The drawing stress of single-pass, (b) the drawing stress of multi-pass, (c) specimen's hardness Hv, vs. the degree of cold work at room temperature for $Ti_{49.7}Ni_{50.3}$ alloy.

2.3 Wire drawing

Figure 13 shows drawing stress and specimen hardness vs. the degree of cold work for tests o $Ti_{49.7}Ni_{50.3}$ alloy done at room temperature. The drawing stress and hardness are found to increase sharply with increasing cold work. This feature reflects the severe work hardening which occurs in TiNi SMAs and which necessitates the interannealing during the drawing process. The defects induced by cold drawing depress the martensitic transformation but promote the R-phase transformation.

Surface oxide films play an important role on the drawing of TiNi SMAs, especially for extra-fine wires[20, 21]. Figures 14 (a), (b) and (c) show the SEM observations of $80\mu m$ ϕ fine TiNi wires after interannealing at 550°C × 10min., 550°C × 70min., and 700°C × 10min., respectively. A thin oxide film with a smooth surface can be used as a lubricant during the drawing process. However, a thick oxide film, which has some cracks and spalling on the surface, hurts the drawing properties and depresses the shape memory effect and pseudoelasticity. Meanwhile, MoS_2 is an effective lubricant for the wire drawing of TiNi shape memory alloys. The drawing stress is lower for the TiNi wires with MoS_2 lubricant and exhibits a quite smooth wire surface after drawing.

3. Damping Characteristics of TiNi Shape Memory Alloys

Figure 15 shows the damping ratio ξ and electrical resistivity vs temperature cruves for the 400°C × 20h aged $Ti_{49}Ni_{51}$ alloy. In Fig. 15, the damping ratio ξ of B19' martensite has nearly the same magnitude as that of the R phase but is larger than that of parent B2 phase. The peaks of damping ratio ξ appear in the temperature ranges of B2↔R and R↔M transformations.

It is well known that there are abundant twin boundaries in the B19' martensite and R phase of TiNi alloys[22, 23]. These twin boundaries can be easily moved by the external stress to accommodate the strain. This accommodation/reorientation phenomenon is closely related to the high damping capacity exhibited in TiNi alloys. As shown in Fig.16, after an elastic response to the stress, an accommodated strain εa in some microdomains can be produced at a critical value of the stress, σa. This strain is due to the stress-induced movement of twin boundaries between the variants of martensite or R phase. The accommodated strain is retained during the unloading but can be reoriented to the opposite direction due to the

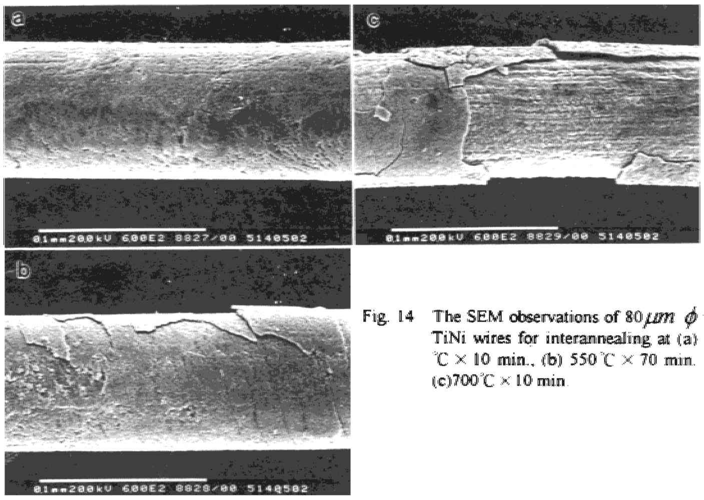

Fig. 14 The SEM observations of 80μm ϕ fine TiNi wires for interannealing at (a) 550 ℃ × 10 min., (b) 550 ℃ × 70 min. and (c)700℃ × 10 min.

movement of twin boundaries induced by the following opposite-direction stress,-σa. This opens up a relatively large static hysteresis loop, ΔW, for the cyclic movement of twin boundaries. Therefore, the martensite and R phase of TiNi alloys have a high-damping capacity which is comparable to or even higher than cast irons[24, 25].

No twin boundaries exist in the parent B2 phase of TiNi alloys, and the dislocation density in the matrix is low[26]. Hence, the damping capacity is suggested simply to come from the dynamic hysteresis of lattice defects, such as vacancies or interstitals. Because the dynamic hysteresis loop generally dissipates a smaller quantity of energy, the damping capacity in the B2 phase of TiNi alloys is smaller than that in martensite R-phase.

In the transformation regions of B2↔M, B2↔R, and R↔M, there are maxima of the damping capacity which are attributed to two contributions. One arises from the plastic strain and twin-interface movement during the thermal-induced transformation. The other originates from the stress-induced transformation formed by the applied external stress.

As shown in Fig.17, all the damping capacities of B19/B19′ martensite, R phase and B2 parent phase for the $Ti_{50}Ni_{49.5}Fe_{0.5}$ and $Ti_{50}Ni_{40}Cu_{10}$ ternary alloys are higher than those for $Ti_{50}Ni_{50}$ binary alloy. The lower yielding stress and shear modulus of these ternary alloys are considered to be responsible for their inherent higher damping property. Noticeably, the $Ti_{50}Ni_{40}Cu_{10}$ alloy has an unusually high plateau of damping capacity in the B19 martensite existing region, which is considered to arise from the easy movement of twin boundaries of B19 martensite due to its inherently very low yielding stress.

4. High Temperature SMAs

Although TiNi alloys are good as practical SMAs, they can not be used at temperatures above about 100℃. Thus, SMAs which can exhibit high temperature SME are strongly demanded. Both $Ti_{50}Ni_{50-x}Pd_x$ and $Ti_{50}Ni_{50-x}Au_x$ alloys with x ≥ 20 at % are quite promising SMAs in the temperature range from 150℃ to 610℃. The transformation temperatures can be easily adjusted from low to high by controlling

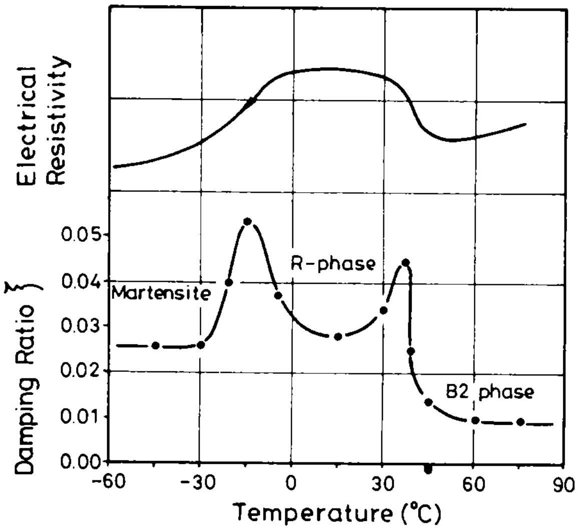

Fig. 15 Damping ratio ξ and electrical resistivity vs temperature curves for the 400℃ × 20h aged $Ti_{49}Ni_{51}$ alloy

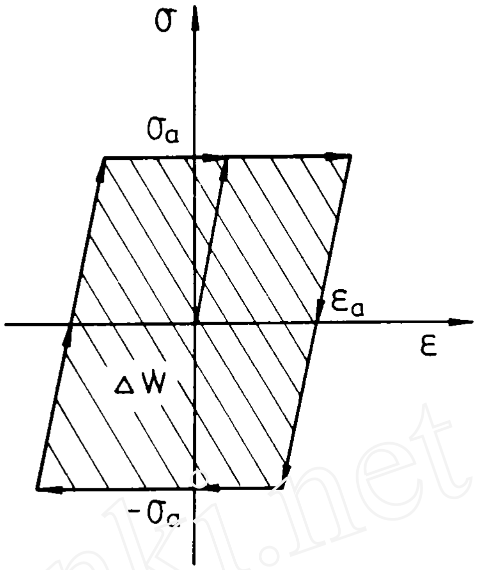

Fig. 16 Schematic stress-strain diagram for the martensite/R-phase accommodation reorientation process. △W indicates the energy loss for the cycling movement of twin boundaries

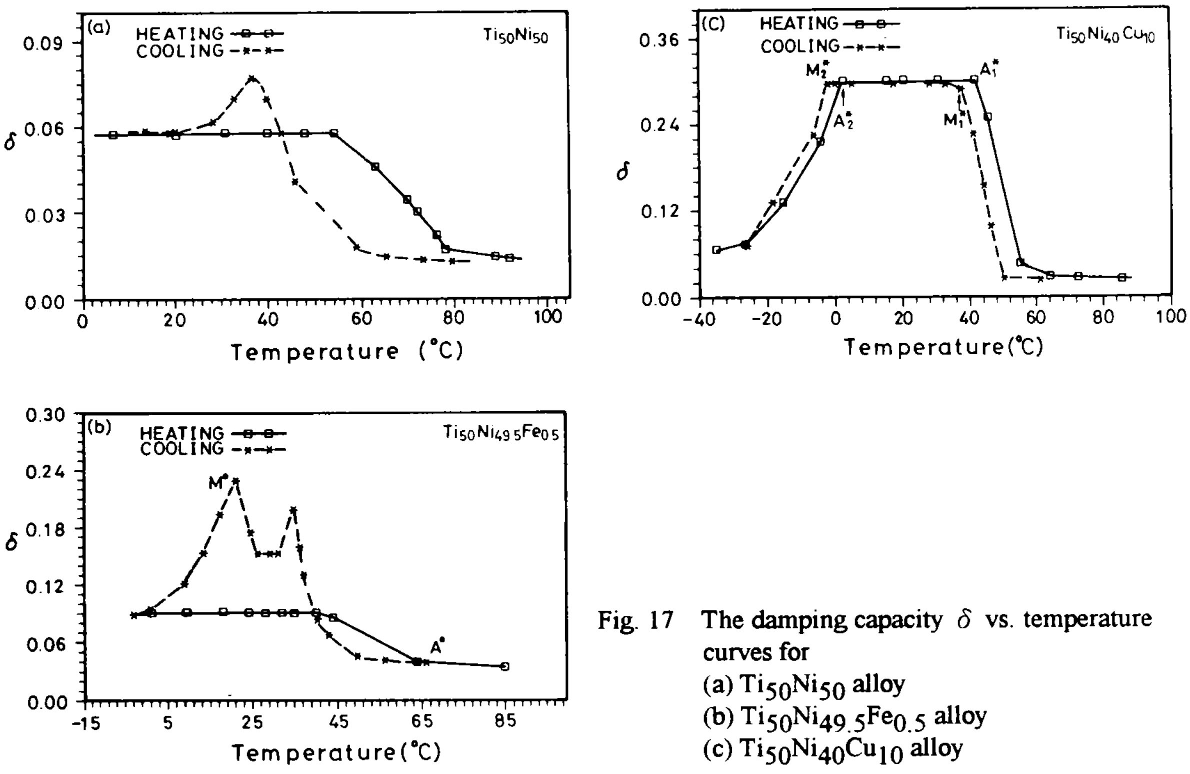

Fig. 17 The damping capacity δ vs. temperature curves for

(a) $Ti_{50}Ni_{50}$ alloy

(b) $Ti_{50}Ni_{49.5}Fe_{0.5}$ alloy

(c) $Ti_{50}Ni_{40}Cu_{10}$ alloy

the added amount of Pd and Au elements, as shown in Fig. 18 for the $Ti_{50}Ni_{50-x}Pd_x$ alloys. Meanwhile, it is worth to say that these high temperature SMAs usually have a one-way SME, but not a two-way SME. This may come from the fact that the accumulated "bias" stresses are released easily when the temperature is raised to above Af dnring the two-way "training" process[27].

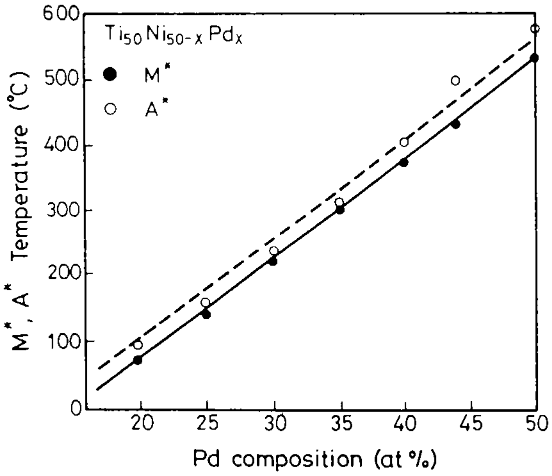

Fig. 18 The M* and A* temperatures vs. Pd composition for the $Ti_{50}Ni_{50-x}Pd_x$ alloys

REFERENCES

1. S. Miyazaki, K. Otsuka and Y. Suzuki, Scripta metall., 1981; 15:287
2. S. Miyazaki, Y. Ohmi, K. Otsuka and Y. Suzuki, ICOMAT-82, J. Phys, 1982; 43: C4-255.
3. S. Miyazaki, T. Imai, Y. Igo and K. Otsuka, Metall. Trans., 1986; 17A: 115
4. H.C. Lin, S.K. Wu and M.T. Yeh, Metall. Trans., 1993; 24A: 2189
5. H.C. Lin, S.K. Wu and Y.C. Chang, Metall. Trans., 1995; 26A: 851
6. C.M. Hwang, M. Meichle, M.B. Salamon and C.M. Wayman, Phil. Mag., 1983; A47: 9, 31
7. T. Todoroki and H. Tamura, Trans. JIM, 1987; 28:83
8. D.N. Abujudom, P.E. Thoma and S.Fariabi, ICOMAT-89, 1990: 565.
9. G. Airoldi, B. Rivolta and C. Turco, ICOMAT-86, 1986: 691.
10. T. Tadaki, Y. Nakata and K. Shimizu, Trans. JIM, 1987; 28: 883
11. K. Iwasaki and R. Hasiguti, Trans. JIM, 1987; 28: 363
12. M. Nishida and C.M. Wayman, Metallography, 1988; 21: 255
13. S.K. Wu, H.C. Lin and T.S. Chou, Acta Metall. Mater., 1990; 38: 95
14. H.C. Lin and S.K. Wu, Scripta Metall. Mater., 1991; 25: 1295
15. Y.C. Lo, S.K. Wu and H.E. Horng, Acta Metall. Mater., 1993; 41: 747
16. H.C. Ling and R. Kaplow, Metall. Trans., 1980; 11A: 77
17. M. B. Salamon, M.E. Meichle and C.M. Wayman, Phys., Rev., 1985; 31B: 7306
18. H.C. Lin and S.K. Wu, Scripta Metall. Mat., 1992; 26: 59
19. H.C. Lin and S.K. Wu, Mat. Sci. and Eng., 1992; A158: 87
20. C.M. Jackson, H.J. Wagner and R.J. Wasilewski, NASA-SP5110, 1972: 19
21. M. Aiba, H. Nagai and M.Asakawa, Materia Japan, JIM, 1992; 31(6): 541 (In Japanese)
22. T.Saburi and S. Nenno, In: Proc. Int. Conf. on Solid to Solid Phase Trans., ASM, Metals Park., OH, 1982: 1455
23. S. Miyazaki and C.M. Wayman, Acta Metall., 1988; 36: 181
24. J.S. Zhu, R. Schaller and W. Benoit, Phys. Satatus Solidi A, 1988; 108: 613
25. K. N. Melton and O. Mercier, Acta Metall., 1980; 29: 393
26. S. Miyazaki and K. Otsuka, Metall. Trans., 1986; 17A: 53
27. S.K. Wu and C.M. Wayman, Metallography, 1987; 20:359